ECCOMAS Congress 2016
VII European Congress on Computational Methods in Applied Sciences and Engineering
M. Papadrakakis, V. Papadopoulos, G. Stefanou, V. Plevris (eds.)
Crete Island, Greece, 5–10 June 2016

CRACK PATH FIELD AND STRAIN INJECTION TECHNIQUES IN DYNAMIC FRACTURE SIMULATIONS

Oriol Lloberas-Valls[1], Alfredo E. Huespe[2], J. Oliver[1] and Ivo F. Dias[3]

[1]CIMNE – Centre Internacional de Metodes Numerics en Enginyeria
Campus Nord UPC, Edifici C-1, c/Jordi Girona 1-3, 08034 Barcelona, Spain
e-mail: olloberas@cimne.upc.edu, xavier.oliver@upc.edu

[2] INTEC-UNL-CONICET
Gemes 3450, Santa Fe, Argentina
e-mail: ahuespe@intec.unl.edu.ar

[3] Laboratório Nacional de Engenharia Civil (LNEC)
Avenida Brasil 101, 1700 Lisbon, Portugal
e-mail: idias@lnec.pt

Keywords: Fracture dynamics, strong discontinuity approach, crack path field, strain injection techniques.

Abstract. *Dynamic fracture phenomena are studied employing low cost computational tools based on Finite Elements with Embedded strong discontinuities (E-FEM). Fracture nucleation and propagation are accounted for through the injection of discontinuous strain and displacement modes inside the finite elements. The Crack Path Field technique is employed to compute the trace of the strong discontinuity during fracture propagation.*

Unstable crack propagation and crack branching are observed upon increasing loading rates. The variation in terms of crack pattern and energy dissipation is studied and a good correlation is found between the maximum experimental crack speed and maximum dissipation at the onset of branching. Comparable results are obtained against simulations employing supra-elemental techniques, such as phase-field and gradient damage models, considering coarser discretizations which can differ by two orders of magnitude.

1 INTRODUCTION

Dynamic fracture processes are challenging phenomena to be studied experimentally. Expensive equipment needs to be employed in order to accurately capture crack growth in a small time frame and dynamic loading conditions are not always straightforward to reproduce in a laboratory.

For this reason, numerical techniques such as Finite element (FE) methods are regarded as valuable alternatives for solving general dynamic fracture problems. However, they show some limitations mainly related with the objectivity, computational cost and the overall ability to predict experimental tests [36]. Different alternatives have been adopted to model crack nucleation and propagation in a dynamic setting. For instance works involving fracture in dynamic problems have been addressed by Falk et al. [7], Pandolfi et al. [26], Song and Belytschko [35] and Linder and Armero [16], where cracks are inserted between FE (inter-elemental) and inside the FE support (intra-elemental). Other techniques tackle the strain localization phenomena by considering supra-elemental bands such as phase-field modeling [2, 11, 19] and gradient damage models [15]. Such techniques led to impressive 2D and 3D results but at the cost of extremely fine FE discretizations which can be regarded prohibitive in a dynamic context where a large amount of time steps need to be resolved in order to capture crack growth with a sufficient time resolution. Softening visco-elastic visco-plastic damage continuum model has been employed for dynamic fracture of concrete up to intermediate loading rates in [27, 28]. At high loading rates, where fragmentation and spalling take place, erosion or element deletion models proposed by Camacho and Ortiz [3], Li et al. [14] have proven to be competitive methods. Other alternative numerical methodologies have been addressed with some success, e.g. peridynamics [10, 32], discrete methodologies such as lattice models [13] and mesh-free methodologies [1], to mention a few.

One of the main objectives of such numerical approaches is to help understanding dynamic fracture phenomena mainly driven by inertial forces which play a dominant role over possible viscous behaviors at high loading rates, e.g. crack curving and branching phenomena detected experimentally when a critical crack tip velocity is exceeded [9, 29–31]. In this scenario, computationally affordable intra-element techniques need to be ready to account for complex fracture patterns in which the dominant crack paths may involve branching and sudden changes of the crack propagation direction.

The present contribution introduces and assesses a finite element method for modeling crack propagation problems with the presence of a dominant crack in brittle or quasi-brittle materials. Problems involving fragmentation or spalling are left outside the scope of this work. Our approach is based on the Embedded Finite Element technology (cf. [4, 23]) which has already been utilized for the study of fracture in quasi-brittle materials and successfully applied to the study of tensile crack growth in gravity dams (cf. [5, 6]). The specific formulation developed by Oliver et al. [24] and assessed for quasi-static multiscale fracture problems has been adopted and tailored for dynamic fracture propagation problems. One of the main advantages of the present approach is that cracks, represented by strong discontinuities embedded into the finite elements, may propagate through the mesh in arbitrary directions reproducing complex failure patterns and, therefore, significantly coarser meshes can be employed compared to other supra-elemental techniques such as phase-field or gradient models.

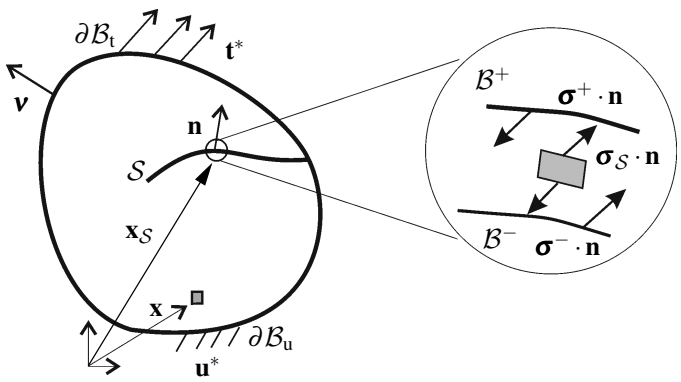

Figure 1: IVBP at solid $\mathcal{B}$ with evolving crack. The disjoint domains of $\mathcal{B}$ generated by $\mathcal{S}$ are denoted $\mathcal{B}^+$ and $\mathcal{B}^-$.

2 MODEL DESCRIPTION

The governing equations of the dynamic fracture Initial Boundary Value Problem (IBVP) at time $t \in [0,T]$ of the solid $\mathcal{B}$ (cf. Figure 1) can be stated as: find $\mathbf{u}$, $\boldsymbol{\varepsilon}$ and $\boldsymbol{\sigma}$, satisfying:

$$\boldsymbol{\nabla}\cdot\boldsymbol{\sigma}+\mathbf{b}=\rho\ddot{\mathbf{u}}\ ; \quad \forall\mathbf{x}\in\mathcal{B}\backslash\mathcal{S}\ ; \quad t\in[0,T]\ ; \quad \text{Momentum equation} \tag{1}$$

$$\boldsymbol{\varepsilon}=\boldsymbol{\nabla}^{\mathrm{s}}\mathbf{u}\ ; \quad \forall\mathbf{x}\in\mathcal{B}\backslash\mathcal{S}\ ; \quad t\in[0,T]\ ; \quad \text{Compatibility equation} \tag{2}$$

$$\boldsymbol{\sigma}=\boldsymbol{\Sigma}(\boldsymbol{\varepsilon},r)\ ; \quad \forall\mathbf{x}\in\mathcal{B}\ ; \quad t\in[0,T]\ ; \quad \text{Constitutive equation} \tag{3}$$

$$\mathbf{u}=\mathbf{u}^*(\mathbf{x},t)\ ; \quad \forall\mathbf{x}\in\partial\mathcal{B}_{\mathrm{u}}\ ; \quad t\in[0,T]\ ; \quad \text{Displ. boundary conditions} \tag{4}$$

$$\boldsymbol{\sigma}\cdot\mathbf{n}=\mathbf{t}^*(\mathbf{x},t)\ ; \quad \forall\mathbf{x}\in\partial\mathcal{B}_{\mathrm{t}}\ ; \quad t\in[0,T]\ ; \quad \text{Traction boundary conditions} \tag{5}$$

$$\mathbf{u}(\mathbf{x},0)=\mathbf{0}\ ; \quad \forall\mathbf{x}\in\mathcal{B}\ ; \quad \text{Initial displ. condition} \tag{6}$$

$$\dot{\mathbf{u}}(\mathbf{x},0)=\dot{\mathbf{u}}_0(\mathbf{x})\ ; \quad \forall\mathbf{x}\in\mathcal{B}\ ; \quad \text{Initial velocity condition} \tag{7}$$

$$\boldsymbol{\sigma}^+\cdot\mathbf{n}=\boldsymbol{\sigma}_{\mathcal{S}}\cdot\mathbf{n}=\boldsymbol{\sigma}^-\cdot\mathbf{n}\ ; \quad \forall\mathbf{x}_{\mathcal{S}}\in\mathcal{S}\ ; \quad t\in[\tau,T]\ ; \quad \text{Traction continuity across } \mathcal{S} \tag{8}$$

where $\mathbf{u}$, $\boldsymbol{\varepsilon}$ and $\boldsymbol{\sigma}$ correspond to the displacement, strain and stress fields and $\mathbf{b}$, ρ and $\boldsymbol{\Sigma}$ denote the volumetric forces, the density and the constitutive relation, respectively. The instant when the discontinuity surface $\mathcal{S}$ is introduced at $\mathbf{x}_{\mathcal{S}}$ is denoted by τ and $\boldsymbol{\sigma}_{\mathcal{S}}$, $\boldsymbol{\sigma}^+$, $\boldsymbol{\sigma}^-$ and $\mathbf{n}$ stand for the stress at an interface point of $\mathcal{S}$, the stresses at each side of this interface and the normal to the discontinuity $\mathcal{S}$.

According to the the Continuum Strong Discontinuity Approach (CSDA) introduced in [21] and [22], the stresses $\boldsymbol{\sigma}_{\mathcal{S}}$ are determined through the constitutive model $\boldsymbol{\Sigma}$ selected for the bulk material accounting for regularization issues.

The strong form of the fracture propagation problem stated in (1) to (8) is recast in a variational format following the methodology presented in [33] and by Oliver et al. [22] where both displacement and strain fields are defined as the addition of a smooth and an enhanced part representing the corresponding singularity in the kinematics. The equivalent variational statement reads:

$$\int_{\mathcal{B}}\boldsymbol{\sigma}:\boldsymbol{\nabla}^{\mathrm{s}}\boldsymbol{\eta}\,d\mathcal{B}+\int_{\mathcal{B}}(\mathbf{b}-\rho\ddot{\mathbf{u}})\cdot\boldsymbol{\eta}\;d\mathcal{B}+\int_{\partial\mathcal{B}_{\mathrm{t}}}\mathbf{t}^*\cdot\boldsymbol{\eta}\;d\Gamma=0 \qquad ;\ \forall\,\boldsymbol{\eta}\ \in\ \hat{\mathcal{V}}_{\mathrm{u}}, \tag{9}$$

where $\mathbf{u}$ and $\boldsymbol{\eta}$ stand for the displacements and displacement variations belonging to the spaces of kinematically admissible displacements $\mathcal{V}_{\mathrm{u}}$ and displacement variations $\hat{\mathcal{V}}_{\mathrm{u}}$, respectively.

2.1 Finite element discretization with different kinematic descriptions

The finite element technology employed in this study is designed to account for different kinematic descriptions which are found optimal to reproduce different stages of fracture nucleation and propagation. Strain localization is considered at the surface $\mathcal{S}$ (cf. Figure 1) which is $k-$regularized in the finite element model, i.e $\mathcal{S}$ is represented by a band of finite thickness k across which the displacements are assumed to be continuous.

Quadrilateral finite elements are employed in all considered discretizations and the resulting mesh is basically divided in two disjoint domains: $\mathcal{B}_{\text{std}}(t)$ and $\mathcal{B}_{\text{inj}}(t)$ ($\mathcal{B} = \mathcal{B}_{\text{std}}(t) \cup \mathcal{B}_{\text{inj}}(t)$) accounting for the standard and injected enhanced kinematics, respectively. These vary with time throughout the evolution of the fracture process as depicted in Figure 2. Domains with injected kinematics $\mathcal{B}_{\text{inj}}(t)$ are, in turn, composed by the union of the disjoint domains $\mathcal{B}_{\text{wd}}$, i.e. with weak discontinuity kinematics, and $\mathcal{B}_{\text{sd}}$, i.e. with strong discontinuity kinematics satisfying $\mathcal{B}_{\text{inj}}(t) = \mathcal{B}_{\text{wd}}(t) \cup \mathcal{B}_{\text{sd}}(t)$. Therefore, three types of domains with different kinematics can be identified in the partitions of $\mathcal{B}$:

1. The domain $\mathcal{B}_{\text{std}}$ corresponds to the union of those finite elements with standard kinematics, i.e. continuous displacements. The finite element formulation employed in $\mathcal{B}_{\text{std}}$ is also termed irreducible formulation since displacements are the only components of the solution field. Bilinear polynomials are used to interpolate the displacement field throughout the quadrilateral elements. The standard kinematics is employed in all FE (belonging to $\mathcal{B}_{\text{std}}$) that are found far away from the main fracture process and, for this reason, no localization phenomena is detected. Due to the standard character of its implementation no further details concerning the formulation of standard kinematics FE are given in this manuscript.

2. The domain $\mathcal{B}_{\text{wd}}$ corresponds to the union of those finite elements in $\mathcal{B}_{\text{inj}}$ where a weak displacement discontinuity is considered in the kinematics. Such kinematic enrichment is also referred to as constant stress-discontinuous strain mode (CS-DSM) in Section 2.1.1 where further formulation details are provided. The weak discontinuity kinematics is employed at regions susceptible of undergoing strain-localization phenomena, i.e. where strains exceed a certain critical threshold. These domains are typically found at a vicinity of the crack tip or in those locations where stress concentration may lead to the nucleation of fracture phenomena. The enhanced deformation of the elements belonging to $\mathcal{B}_{\text{wd}}$, amenable to carry a non-directional discontinuity, renders a flexible element which is particularly useful to determine the correct propagation of the crack and to accommodate the strain states at crack branching regions.

3. The domain $\mathcal{B}_{\text{sd}}$ corresponds to the union of those finite elements in $\mathcal{B}_{\text{inj}}$ in which a strong displacement discontinuity is considered in the kinematics. Such kinematic enrichment is also referred to as discontinuous displacement mode (DDM) in Section 2.1.2 where further formulation details are provided. The strong discontinuity kinematics is employed throughout the trace of the crack and the elements belonging to $\mathcal{B}_{\text{sd}}$ must exceed a certain strain threshold and, additionally, fulfill a number of conditions, detailed in Section 2.1.2.

The domain $\mathcal{B}_{\text{inj}}$ is, therefore, modeled with finite elements equipped with strain injections, including CS-DSM and DDM modes introduced in [18, 24]. Strain injections are included in finite elements through the concept of assumed enhanced strains [34] considering a three-field Petrov-Galerkin mixed formulation by assuming that displacements $\mathbf{u}$ and strains $\boldsymbol{\varepsilon}$ in (9) are

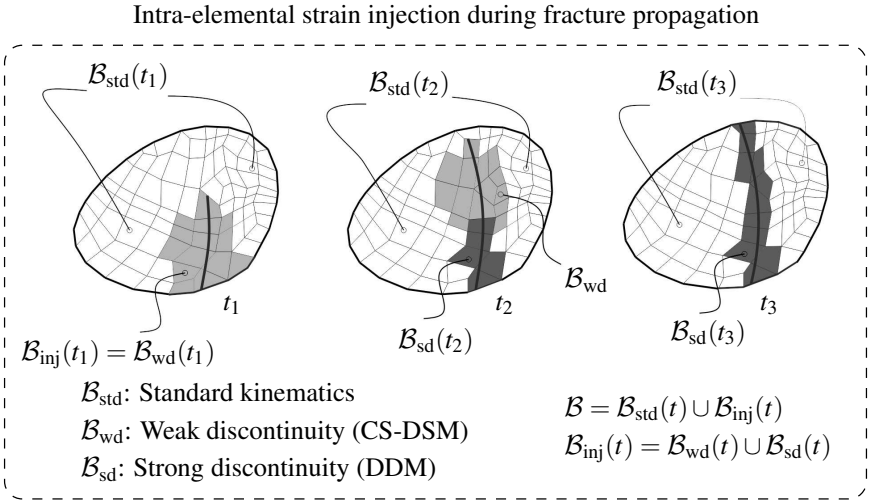

Figure 2: Subdomain categories of the discrete body along different times (t_1, t_2 and t_3) of the analysis.

independent fields. In both CS-DSM and DDM modes the strain field is partitioned in two terms: $\boldsymbol{\varepsilon} = \boldsymbol{\xi} + \boldsymbol{\gamma}$ denoting a compatible (and smooth) strain field $\boldsymbol{\xi}$ and an enhanced strain field $\boldsymbol{\gamma}$ which tackles possible singularities in the failure propagation kinematics.

The resulting Embedded Finite Element method (E-FEM) has been already presented in [23] and [24] and assessed for the case of quasi-static failure propagation. In the following subsections a brief description of its formulation is given but the reader is referred to the works in [18, 23, 24] for complete implementation details.

2.1.1 Weak discontinuity injection in $\mathcal{B}_{\text{wd}}$. Constant Stress-Discontinuous Strain Mode (CS-DSM)

The weak discontinuity kinematics is injected when a user defined strain threshold is exceeded (cf. [18]). Such critical strain threshold is determined based on a strain-like internal variable of the damage model, r, which records the maximum historical value of the equivalent strain, τ_ε, accounting for the positive strain counterpart, i.e. only tensile stress states contribute to the strain norm. For complete details on the k-regularized damage model employed in this study the reader is referred to the works in [8, 18, 20].

Considering the strain field decomposition into a compatible and enhanced strain, the resulting variational three-field problem can be stated as: Find $\mathbf{u} \in \mathcal{V}_{\text{u}}^{\text{wd}}$ and $\boldsymbol{\varepsilon} = \boldsymbol{\xi} + \boldsymbol{\gamma}$ with $\boldsymbol{\xi} \in \mathcal{V}_{\varepsilon}^{\text{wd}}$ and $\boldsymbol{\gamma} \in \mathcal{V}_{\gamma}^{\text{wd}}$, satisfying:

$$\int_{\mathcal{B}} \boldsymbol{\sigma}(\boldsymbol{\varepsilon}) : \boldsymbol{\nabla}\boldsymbol{\eta}\, d\mathcal{B} - \underbrace{\int_{\mathcal{B}} (\mathbf{b} - \rho\ddot{\mathbf{u}}) \cdot \boldsymbol{\eta}\, d\mathcal{B} - \int_{\partial\mathcal{B}_{\text{t}}} \mathbf{t}^* \cdot \boldsymbol{\eta}\, d\Gamma}_{\mathbf{W}_{\eta}^{\text{ext}}(\boldsymbol{\eta},\mathbf{b},\ddot{\mathbf{u}},\mathbf{t}^*)} = 0; \qquad \forall \boldsymbol{\eta} \in \hat{\mathcal{V}}_{\text{u}}^{\text{wd}}, \tag{10}$$

$$\int_{\mathcal{B}^e} \phi^e \hat{\boldsymbol{\xi}}^e : \left(\phi^e \boldsymbol{\xi}^e - \sum_{i=1}^{n^e_{\text{node}}} (\boldsymbol{\nabla}^{\text{s}} N_i^e \otimes \mathbf{d}_i^e) \right) d\mathcal{B} = 0; \qquad \forall \hat{\boldsymbol{\xi}}^e \in \hat{\mathcal{V}}_{\varepsilon}^{\text{wd}}, \tag{11}$$

$$\int_{\mathcal{B}^e} \hat{\boldsymbol{\gamma}}^e : (\boldsymbol{\chi}_S^{(h^e,k^e)} \boldsymbol{\sigma})\, d\mathcal{B} = \int_{\mathcal{S}^e} \hat{\boldsymbol{\gamma}}^e : [\![\boldsymbol{\sigma}]\!]\, d\mathcal{B} = 0; \qquad \forall \hat{\boldsymbol{\gamma}}^e \in \hat{\mathcal{V}}_{\gamma}^{\text{wd}}, \tag{12}$$

where $\mathcal{V}_{\square}^{\text{wd}}$ and $\hat{\mathcal{V}}_{\square}^{\text{wd}}$ denote the trial and test function spaces, respectively. The subindices u, ε and γ refer to the spaces of displacements $\mathbf{u}$, strains $\boldsymbol{\varepsilon}$ and enhanced strain fields $\boldsymbol{\gamma}$, respectively (cf. [18] for a detailed definition of these function spaces). Displacements $\mathbf{u}$ and displacement variations $\boldsymbol{\eta}$ are element-wise interpolated using standard bilinear shape functions while the compatible and enhanced strain components are interpolated using the spatially constant function ϕ and the dipole function χ, detailed in [18, 24]. The term denoted $\mathbf{W}_{\eta}^{\text{ext}}$ in (10), refers to the virtual work due to the external and inertial forces.

As described in [18] the non-directional character of the strain enhancement renders the CS-DSM element an excellent candidate to be employed at regions undergoing complex fracture phenomena such as crack branching and intersection. It is designed to sense strain localization phenomena and, therefore, is seen particularly useful to anticipate a strong discontinuity at the crack tip region in a certain well-captured propagation direction.

2.1.2 Strong discontinuity injection in $\mathcal{B}_{\text{sd}}$. Discontinuous Displacement Mode (DDM)

Upon increasing strain localization in a particular direction, the strong discontinuity kinematics is injected after the the injection of the weak discontinuity. The element to be enriched with the strong discontinuity kinematics belongs to $\mathcal{B}_{\text{inj}}$ for which the strain threshold referred in Section 2.1.1 must have been exceeded. Additionally, all elements in $\mathcal{B}_{\text{sd}}$ must fulfill the following conditions (cf. [18] for a more detailed explanation):

1. The constitutive tangent satisfies the bifurcation condition, i.e. the determinant of the corresponding acoustic tensor must vanish.

2. The local dissipation per unit of surface exceeds a user-defined fraction of the material fracture energy G_{f}

3. The trace of one strong discontinuity $\mathcal{S}$ (cf. Section 2.2) intersects the element.

When the above mentioned conditions are accomplished, the strong discontinuity kinematics can be injected with confidence propagating the crack following a correct direction and avoiding possible stress locking effects arising from any kinematic incompatibilities.

Considering the strain field decomposition into a compatible and enhanced strain field, as proposed in the assumed enhanced strains methodology, the mixed variational problem in $\mathcal{B}_{\text{sd}}$ can be written as: find $\mathbf{u} \in \mathcal{V}_{\text{u}}^{\text{sd}}$ and $\boldsymbol{\varepsilon}_{\text{sd}} = \boldsymbol{\xi}_{\text{sd}} + \boldsymbol{\gamma}_{\text{sd}}$ with $\boldsymbol{\xi}_{\text{sd}} \in \mathcal{V}_{\varepsilon}^{\text{sd}}$ and $\boldsymbol{\gamma}_{\text{sd}} \in \mathcal{V}_{\gamma}^{\text{sd}}$, satisfying:

$$\int_{\mathcal{B}} \boldsymbol{\sigma}(\boldsymbol{\varepsilon}) : \boldsymbol{\nabla}^{\text{s}} \boldsymbol{\eta} \, d\mathcal{B} - \mathbf{W}_{\eta}^{\text{ext}}(\boldsymbol{\eta}, \mathbf{b}, \ddot{\mathbf{u}}, \mathbf{t}^{*}) = 0; \qquad \forall \boldsymbol{\eta} \in \hat{\mathcal{V}}_{\text{u}}^{\text{sd}}, \tag{13}$$

$$\int_{\mathcal{B}^e} \chi_S^{+}(\mathbf{x}) \, (\llbracket \hat{\mathbf{u}} \rrbracket^e \otimes^{\text{s}} \mathbf{n} : \boldsymbol{\sigma}) \, d\mathcal{B} = \int_{\mathcal{S}^e} \llbracket \hat{\mathbf{u}} \rrbracket^e \cdot \llbracket \boldsymbol{\sigma} \cdot \mathbf{n} \rrbracket \, d\Gamma = 0; \qquad \forall \llbracket \hat{\mathbf{u}} \rrbracket^e \in \mathbb{R}^{n_{\text{dim}}}, \tag{14}$$

$$\int_{\mathcal{B}^e} \phi^e \hat{\boldsymbol{\xi}}_{\text{sd}}^{\,e} : \left(\phi^e \boldsymbol{\xi}_{\text{sd}}^{\,e} - \left[\boldsymbol{\nabla}^{\text{s}} N_i^e \otimes \mathbf{d}_i^e) - \boldsymbol{\nabla} \boldsymbol{\varphi}^e \otimes^{\text{s}} \llbracket \mathbf{u} \rrbracket^e \right] \right) d\mathcal{B} = 0; \qquad \forall \hat{\boldsymbol{\xi}}^{\,e} \in \mathbb{S}^{n_{\text{dim}} \times n_{\text{dim}}}, \tag{15}$$

where $\mathcal{V}_{\square}^{\text{sd}}$ and $\hat{\mathcal{V}}_{\square}^{\text{sd}}$ denote the trial and test function spaces, respectively. The subindices u, ε and γ refer to the spaces of displacements $\mathbf{u}$, strains $\boldsymbol{\varepsilon}$ and enhanced strain fields $\boldsymbol{\gamma}$, respectively (The reader is referred to the work in [18] for a detailed definition of these function spaces).

Displacements variations $\boldsymbol{\eta}$ are element-wise interpolated using standard bilinear shape functions while the displacements $\mathbf{u}$ are interpolated as an addition of a standard interpolation of the smooth term and a term accounting for the displacement jump $[\![\mathbf{u}]\!]$ through the Heaviside step function and an element auxiliary function described in [18, 24]. The compatible strain and compatible strain variations are interpolated using the spatially constant function ϕ. The enhanced strains are element-wise interpolated employing the dirac delta shifted to $\mathcal{S}$ and the enhanced strain variations are computed through the generalized dipole-like function χ_S^+ detailed in [18, 24].

2.2 Crack Path Field tracking algorithm

The trace of the strong discontinuity is computed through the crack path field (CPF) technique introduced by Oliver et al. [23]. Essentially, a directional maximum of a conveniently chosen localizing field r (cf. [18, 23, 24]) is calculated defining the so-called crack path set Γ, i. e. predicting the trace of the strong discontinuity $\mathcal{S}$.

The direction in which the maximum of r is identified is taken according to the vector field

$$\hat{\mathbf{e}}(\mathbf{x},t) = \frac{\boldsymbol{\nabla}\tilde{u}(\mathbf{x},t)}{||\boldsymbol{\nabla}\tilde{u}||} \tag{16}$$

where $\tilde{u}$ denotes a scalar value of the displacement field $\mathbf{u}$ (cf. [18]). The orientation of the strong discontinuity $\mathbf{n}$ is directly taken from the vector $\hat{\mathbf{e}}$. The directional maximum of r, identifying the crack path set Γ, is computed through the zero-level set of the so called crack path field $\mu(\mathbf{x},t)$, defined as:

$$\mu(\mathbf{x},t) = \frac{\partial \tilde{r}}{\partial e} = \boldsymbol{\nabla}\tilde{r}\cdot\hat{\mathbf{e}}, \tag{17}$$

where $\tilde{r}$ is a sufficiently smooth field of r. The zero-level set of μ defines the crack path set Γ as

$$\Gamma(t) := \{\mathbf{x} \quad \big| \mu(\mathbf{x},t) = \frac{\partial \tilde{r}}{\partial e} = 0\}. \tag{18}$$

Note that $\mathcal{S}$ is contained in the crack path set Γ (cf. Figure 3) and is identified as the portion of Γ belonging to $\mathcal{B}_{\text{sd}}$. Once the intersections between $\mathcal{S}$ and the finite element boundaries are known, the auxiliary function φ^{e} can be constructed.

The spirit of the CPF technique is to facilitate the computation of the trace of the strong discontinuity specially in those cases in which crack propagation may be biased by mesh alignment or structured discretizations (cf. [23]).

2.3 Implicit time integration

The enhanced degrees of freedom ($\bar{\boldsymbol{\xi}}^e$ and $\bar{\boldsymbol{\gamma}}^e$ in (10)–(11), or $\bar{\boldsymbol{\xi}}^e$ and $[\![\mathbf{u}]\!]^e$ in (13)–(15)) are condensed out at the element level and, therefore, the unknowns in the discrete model consist on the vector of smooth displacements $\mathbf{u}$ and accelerations $\ddot{\mathbf{u}}$. Consequently, the elements with enhanced kinematics do not lead to an increase of the standard degrees of freedom. Since the enhanced degrees of freedom do not have an associated mass, their condensation is performed as done in quasi-static problems.

The resulting global system of equations in terms of $\mathbf{u}$ for each time step can be written in a matrix form as:

$$\mathbf{M}\ddot{\mathbf{u}}(t) + \mathbf{F}_{\text{int}}(\mathbf{u}(t)) - \mathbf{F}_{\text{ext}}(t) = \mathbf{0}, \tag{19}$$

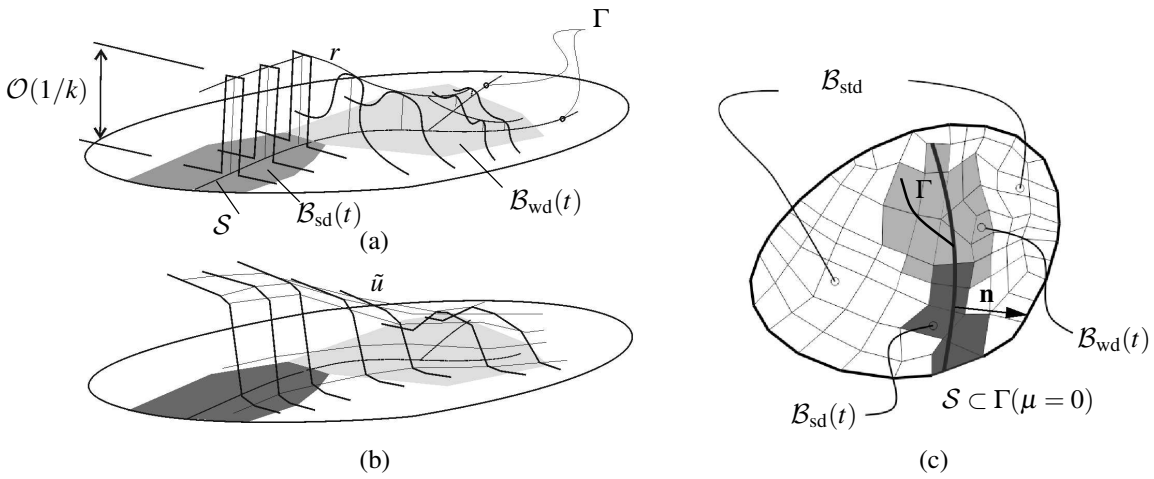

Figure 3: Crack Path Field (CPF) strategy for the crack tracking algorithm. Γ denotes the crack path set. (a) Localized field r around a strong discontinuity band. (b) Associated scalar displacement field $\tilde{u}$. (c) Γ (zero-level set of the crack path field function $\tilde{\mu}$) and the trace of the strong discontinuity $\mathcal{S}$.

where $\mathbf{M}$ and $\mathbf{F}_{\text{ext}}$ represent the mass matrix and external force vector, without the inertial forces, respectively. The mass matrix is computed in a standard way, i.e. lumping the contributions to a diagonal matrix, and is only associated to the degrees of freedom of the smooth displacement field. The internal force vector and $\mathbf{F}_{\text{int}}$ results from the evaluation of the first term, on the l.h.s. of (9), (10) or (13), corresponding to $\mathcal{B}_{\text{std}}$, $\mathcal{B}_{\text{wd}}$ and $\mathcal{B}_{\text{sd}}$, respectively.

A standard implicit time integration (Newmark) scheme is employed to find the solution of (19) at time step $t+1$. Considering the solution $\mathbf{u}^{t+1}$ the system of equations in (19) can be expressed as

$$\mathbf{R}(\mathbf{u}^{t+1}) = \mathbf{0}. \tag{20}$$

Due to the evolution of crack phenomena, the integration domains vary with time, as well as the spatial integration rules and the residual force vector has to be evaluated in an incremental way as follows:

$$\mathbf{R}(\mathbf{u}^{t+1}) = \mathbf{R}(\mathbf{u}^{t}) + \Delta\mathbf{R}\Big(\Delta\mathbf{u}^{t+1}, \mathcal{B}^{t}_{\text{std}}, \mathcal{B}^{t}_{\text{wd}}, \mathcal{B}^{t}_{\text{sd}}\Big). \tag{21}$$

The integration rules for the evaluation of the residual force vector, $\mathbf{R}$, are specific for each domain $\mathcal{B}^{t+1}_{\text{std}}$, $\mathcal{B}^{t+1}_{\text{wd}}$ and $\mathcal{B}^{t+1}_{\text{sd}}$. An alternative approach is utilized in our implementation which consists in redefining the stresses, which take place in the internal force expressions such that one quadrature rule suffices for evaluating $\mathbf{R}(\mathbf{u}^{t+1})$ in the complete domain $\mathcal{B}$ (cf. Oliver et al. [23, 24] for details of the effective stress definition and their updating scheme).

3 Representative simulations

The following examples illustrate the performance of the crack path field and strain injection techniques in dynamic simulations with different loading rates and material brittleness. Plane strain conditions are assumed in all two-dimensional examples.

3.1 Dynamic simulations of quasi-brittle fracture at different loading rates

Dynamic fracture simulations of a compact tension (CT) test are performed considering a quasi-brittle material such as concrete (cf. Figure 4). The influence of the loading regime is studied by varying the pressure rates applied at the loading walls of the CT specimen. The damage model described in [17, 24] is employed with a linear softening law and an only tension

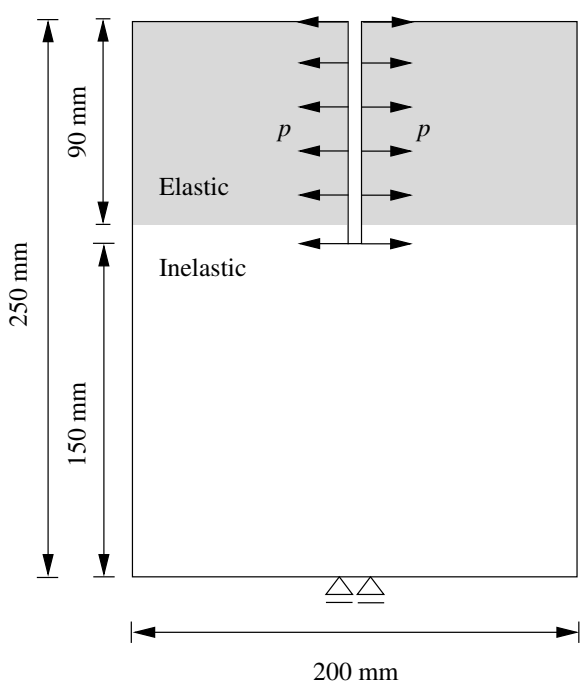

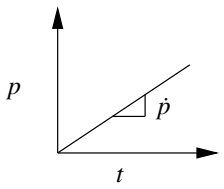

	$\dot{p}\left[\frac{N}{mm^2 \cdot s}\right]$
Low loading rate	1.077×10^3
Medium loading rate	$7.180 - 10.000 \times 10^3$
High loading rate	$13.067 - 21.538 \times 10^3$

Figure 4: Geometry and boundary conditions for the dynamic CT test.

$\sigma_u\ [N/mm^2]$	E $[N/mm^2]$	ν	$G_f\ [N/mm]$	$\rho\ [Kg/m^3]$
3.5	30.0×10^3	0.18	0.09	2400

Table 1: Material parameters for the dynamic compact tension (CT) test.

failure criterion. A constant time discretization is considered with $\Delta t = 10^{-6}$ s and the material parameters are shown in Table 1.

In order to prevent damage nucleation at the vicinity of the wall where the pressure load is applied, the upper part of the specimen (cf. Figure 4) is kept elastic. The Rayleigh wave speed v_R for a concrete material is considered approximately equal to 2100 m/s (cf. [25]).

Upon increasing loading rate, the failure pattern changes from a vertical mode-I crack to mixed mode with multiple cracks, i.e. the fracture surface increases (cf. Figure 5). This tendency is also observed in Ožbolt et al. [25] where a similar test is studied. The injection of weak and strong discontinuities in combination with the Crack Path Field (CPF) tracking algorithm automatically captures branching phenomena without the need for a special strong discontinuity kinematics at the branched element as proposed in [16]. In the proposed methodology, the crack path sets cannot intersect itself and, therefore, the elements at the branching region are injected with the CS-DSM which has no assumed direction of localization.

The total energy dissipation and the dissipation plots are shown for different loading rates $\dot{p}$ ranging 1.077×10^3 to $2.154 \times 10^4\ N/mm^2/s$ in Figure 6. Such dissipated energy $W^{\mathcal{D}}$ at time t is calculated as:

$$W^{\mathcal{D}}(t) = \int_0^t P_{\text{ext}}(t)\, dt - \Psi(t) - \mathcal{K}(t), \tag{22}$$

where $P_{\text{ext}}(t)$ denote the external mechanical power, performed by the external loads excluding the inertial forces, $\Psi(t)$ the total internal energy and $\mathcal{K}(t)$ the kinetic energy, at time t. Addi-

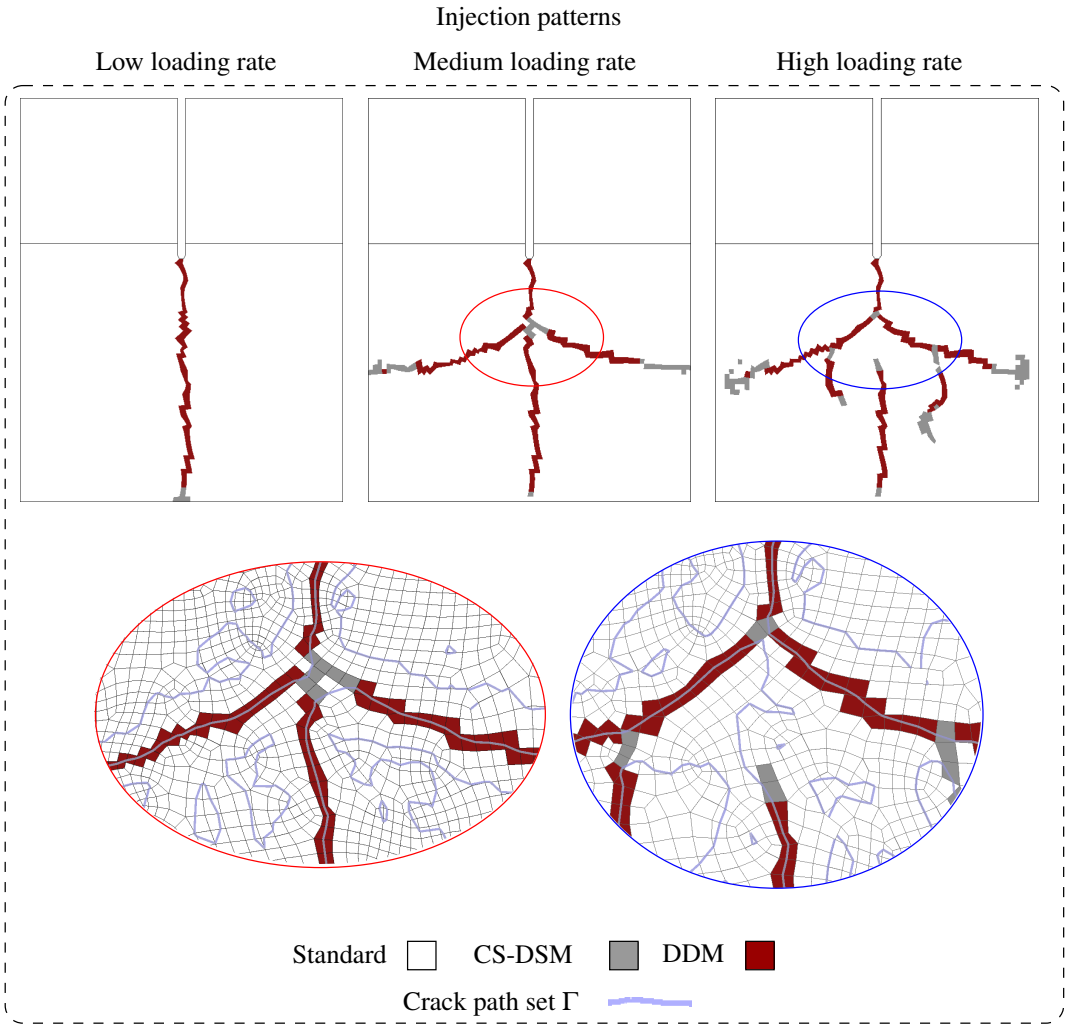

Figure 5: Injection patterns upon increasing loading rate at the dynamic compact tension test.

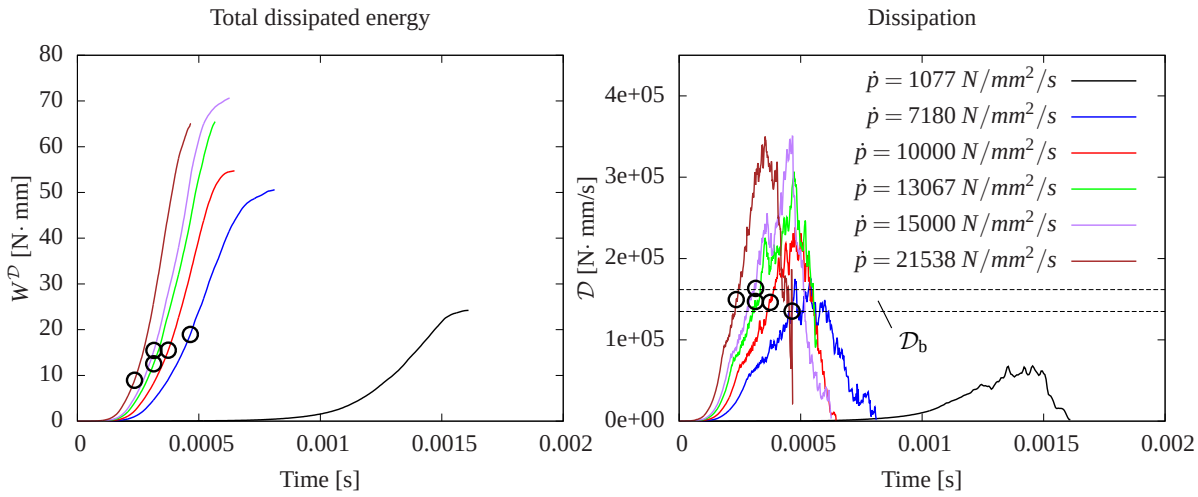

Figure 6: Time evolution of the total dissipated energy (left) and dissipation (right) for different loading rates. The black circles indicate the first observed branching episode. A thickness of 1mm is considered for the energy plots.

tionally, the dissipation $\mathcal{D}(t)$ can be computed as the derivative with respect to time of $W^{\mathcal{D}}(t)$ since

$$W^{\mathcal{D}}(t) = \int_0^{\chi=t} \mathcal{D}(\chi)\, d\chi. \tag{23}$$

The total dissipated energy and crack surface increase upon increasing loading and the corresponding dissipation presents a higher peak value (cf. Figure 6). The branching episodes are indicated in the plots with black circles at each of the curves. It is observed that all dissipations measured during branching events cluster in a region between 1.35×10^5 and 1.62×10^5 $N \cdot mm/s$. These limits $\mathcal{D}_\mathrm{b}$ can be estimated as

$$\mathcal{D}_\mathrm{b} = v_\mathrm{b} G_\mathrm{f} k, \tag{24}$$

where v_b refers to the crack velocity at the onset of branching reported in experiments, i.e. between 500 and 600 m/s for concrete material [25], G_f stands for the material fracture energy and k denotes the considered bandwidth of the localization zone in the DDM (cf. [18, 23]).

The expression in (24) implicitly sets a maximum dissipation for a single crack considering that the energy is instantaneously dissipated. In this view, all registered dissipations greater than the estimated upper limit in (24) necessarily involve more than one crack. In all results shown in Figure 6 the dissipations registered upon the onset of branching fit reasonably well between the above mentioned limits computed with the experimental maximum crack velocities 500 and 600 m/s.

For this reason, the expression in (24) can be seen as a methodology to infer the crack velocity at the onset of branching knowing the total dissipation assuming that the energy is instantaneously released during crack propagation. Considering the upper and lower registered dissipation limits at the onset of branching, the corresponding limiting velocities are 501.82 and 545.58 m/s according to (24). This alternative approach is based on the global dissipation values field $\mathcal{D}$ which is remarkably smoother and reliably evaluated than the crack tip velocity field.

In [11], crack branching is detected when a critical crack surface rate is reached which is analogous to the dissipation criteria. However, the advantage of monitoring the rate of dissipated energy is that it can be performed by accounting for a global energy balance instead of

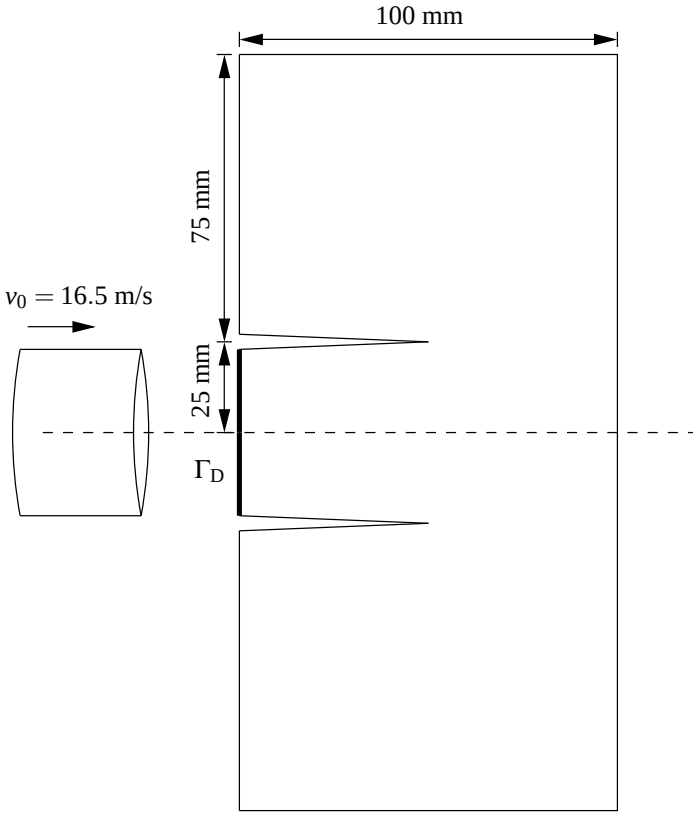

Figure 7: Geometry and boundary conditions for the Kalthoff experiment.

$\sigma_u\ [N/mm^2]$	E $[N/mm^2]$	ν	$G_f\ [N/mm]$	$\rho\ [Kg/m^3]$
844.0	190.0×10^3	0.3	22.17	8000

Table 2: Material parameters and wave velocities for the Kalthoff experiment.

locally studying crack surface growth. In other words, the total energy dissipation is computed as the difference between the external loads energy minus the deformation and kinetic energies. In this way, no additional model-dependent criteria are needed to locate the crack tip position.

3.2 Towards simulations of brittle failure involving complex fracture phenomena

The strain injection and crack path field techniques are employed to reproduce the Kalthoff experiment [12] (cf. Figure 7) consisting of an edged-cracked plate impacted by a projectile. It is reported experimentally that, at an impact velocity $v_0 = 16.5\ m/s$, a mode I crack propagates from the notch towards the superior and inferior specimen edges at an angle of proximately 70 degrees.

An applied velocity at the prescribed contour Γ_D mimics the boundary condition resulting from the impact. The test is imposed on a metallic plate with material parameters summarized in Table 2. Both unstructured and structured meshes have been studied with approximately 15000 elements and a time step discretization $\Delta t = 10^{-7}$ s is adopted.

Injection patterns for both meshes shown in Figure 8 reveal that both results are very much comparable and in agreement with the experimental results which report crack propagation an-

gles close to 70 degrees. The patterns are remarkably symmetric as expected from the imposed boundary conditions and are found in agreement with those provided by different numerical techniques, e.g. phase-field [11] and gradient damage models [15] but at the expense of a mesh discretization which is around two orders of magnitude finer (cf. Figure 9).

4 Conclusions

A FE formulation is presented which is capable of tackling fracture dynamics problems through the injection of weak and strong displacement discontinuities. Since the kinematic enhancement simulating the fracture is performed inside the element (intra-elemental) and not represented by bandwidth of several elements (supra-elemental), the necessary FE discretization can be adopted significantly coarser than strategies such as phase field or gradient damage models.

The crack path field global tracking technique in combination with the strong discontinuity injection procedure automatically account for complex fracture phenomena encountered upon increasing loading rates such as branching. Crack branching regions are injected with the non-directional CS-DSM element while the rest of the trace of discontinuity is modeled with the strong discontinuity injection.

Assuming that the fracture energy is instantly released, the maximum dissipation for one propagating crack can be estimated as the product of the fracture energy, the maximum crack tip velocity and the crack band width. In this view, the crack branching velocities can be estimated by monitoring the dissipation at the onset of branching $\mathcal{D}_{\mathrm{b}}$ and have been found to be in good agreement with crack tip velocities at the onset of branching reported experimentally.

The simulation of the Kalthoff experiment with both structured and unstructured meshes provides results in agreement with other supra-elemental numerical schemes but employing a finite element discretization which can be up to two orders of magnitude coarser.

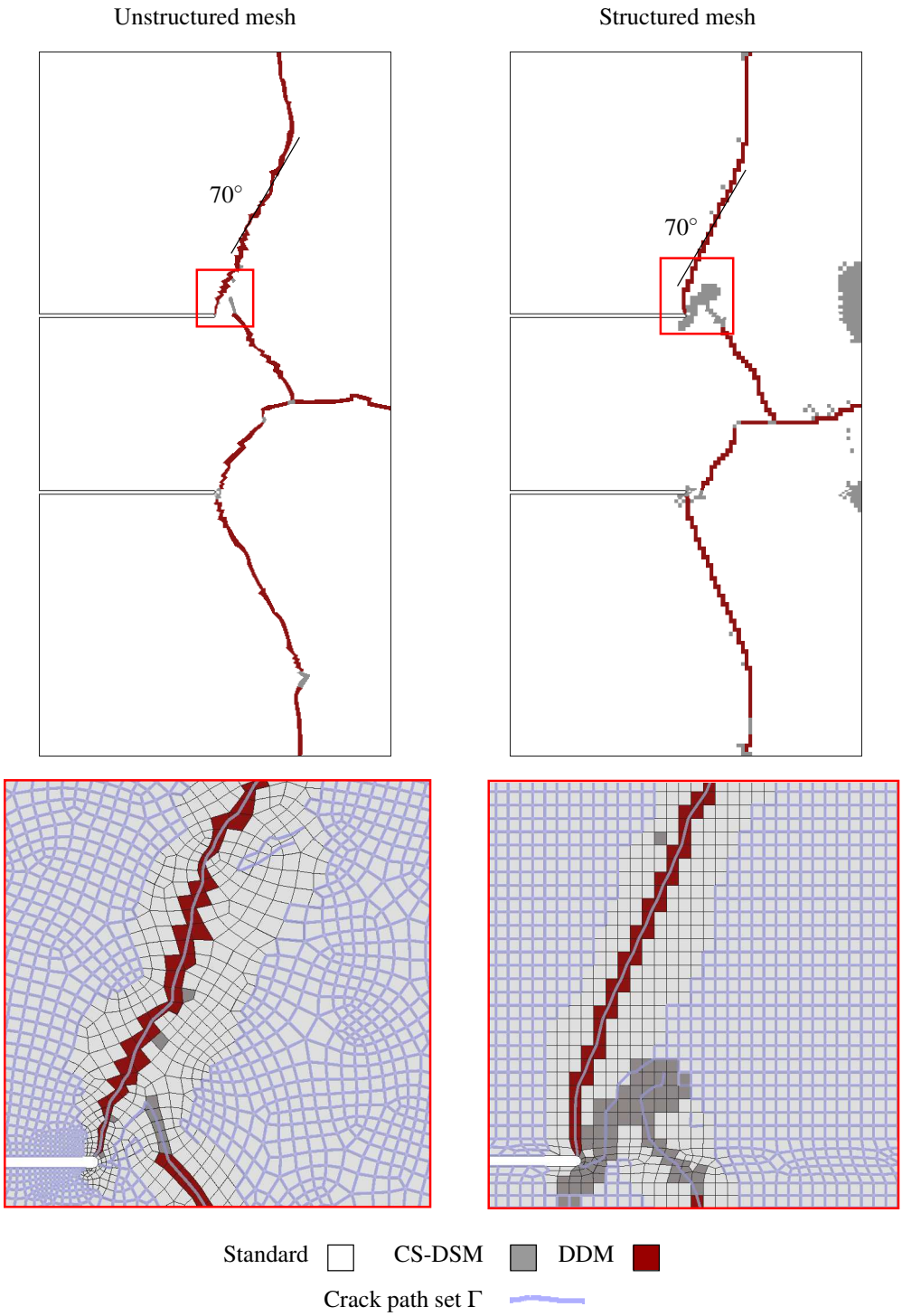

Figure 8: Injection patterns for the unstructured and structured meshes.

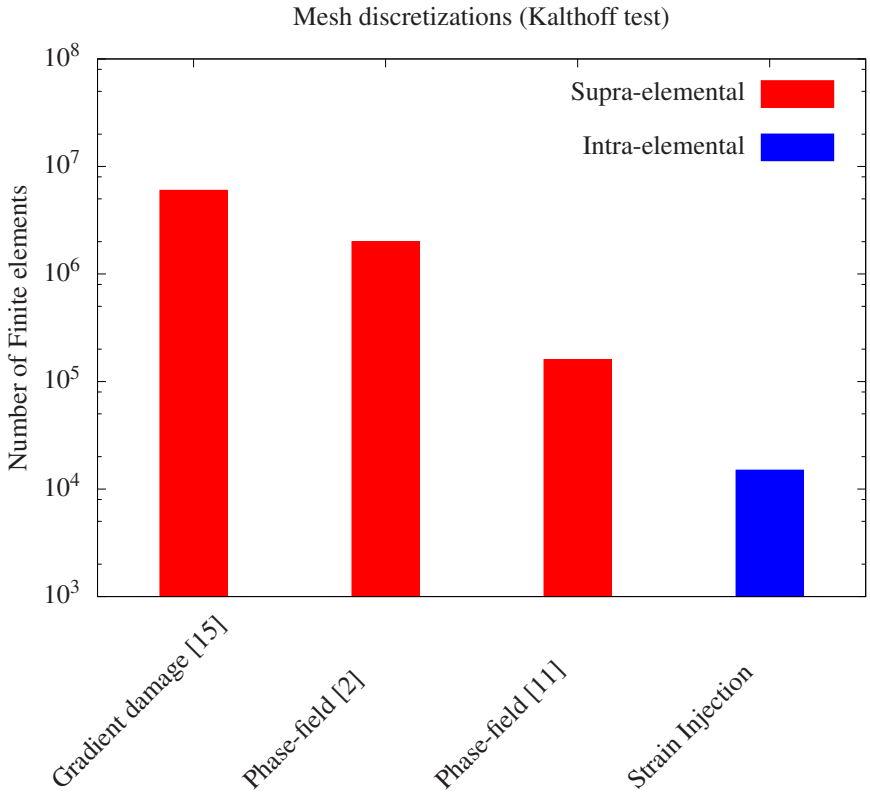

Figure 9: Equivalent mesh discretizations for the Kalthoff experiment employing different numerical techniques.

Acknowledgments

The research leading to these results has received funding from the European Research Council under the European Union's Seventh Framework Programme (FP/2007-2013) / ERC Grant Agreement n. 320815 (ERC Advanced Grant Project "Advanced tools for computational design of engineering materials" COMP-DES-MAT). Oriol Lloberas-Valls gratefully acknowledges the funding received from the Spanish Ministry of Economy and Competitiveness through the "Juan de la Cierva" Postdoctoral Junior Grant: JCI-2012-13782 and the National Research Plan 2014: MAT2014-60919-R. Ivo Dias gratefully acknowledges the financial support from Laboratório Nacional de Engenharia Civil (LNEC) through the postdoctoral research Grant (CoMatFail project).

References

[1] T. Belytschko, D. Organ, and C. Gerlach. Element-free galerkin methods for dynamic fracture in concrete. *Computer Methods in Applied Mechanics and Engineering*, 187(3–4):385–399, 2000.

[2] M. J. Borden, C. V. Verhoosel, M. A. Scott, T. J. R. Hughes, and C. M. Landis. A phase-field description of dynamic brittle fracture. *Computer Methods in Applied Mechanics and Engineering*, 217220:77 – 95, 2012.

[3] G. T. Camacho and M. Ortiz. Computational modelling of impact damage in brittle materials. *International Journal of Solids and Structures*, 33(2022):2899–2938, 1996.

[4] I. F. Dias, J. Oliver, and A. E. Huespe. *Strain Injection Techniques in Numerical Modeling*

of Propagating Material Failure. Monograph. International Center for Numerical Methods in Engineering, 2012. ISBN 978-84-940243-7-5.

[5] I. F. Dias, J. Oliver, J. V. Lemos, and O. Lloberas-Valls. Advanced numerical techniques for modeling tensile crack propagation in gravity dams. In *Second International Dam World Conference*. LNEC, Lisbon, Portugal, 2015.

[6] I. F. Dias, J. Oliver, J. V. Lemos, and O. Lloberas-Valls. Modeling tensile crack propagation in concrete gravity dams via crack-path-field and strain injection techniques. *Engineering Fracture Mechanics*, 2016. In press.

[7] M. L. Falk, A. Needleman, and J. R. Rice. A critical evaluation of cohesive zone models of dynamic fractur. *Le Journal de Physique IV*, 11(PR5):Pr5–43, 2001.

[8] R. Faria, J. Oliver, and M. Cervera. A strain-based plastic viscous-damage model for massive concrete structures. *International Journal of Solids and Structures*, 35(14):1533–1558, 1998.

[9] L. B. Freund. *Dynamic Fracture Mechanics*. Cambridge University Press, 1998.

[10] Y. Ha and F. Bobaru. Studies of dynamic crack propagation and crack branching with peridynamics. *International Journal of Fracture*, 162(1–2):229–244, 2010.

[11] M. Hofacker and C. Miehe. A phase field model of dynamic fracture: Robust field updates for the analysis of complex crack patterns. *International Journal for Numerical Methods in Engineering*, 93(3):276–301, 2013.

[12] J. Kalthoff. Modes of dynamic shear failure in solids. *International Journal of Fracture*, 101(1-2):1–31, 2000.

[13] L. Kosteski, R.B DAmbra, and I. Iturrioz. Crack propagation in elastic solids using the truss-like discrete element method. *International journal of fracture*, 174(2):139–161, 2012.

[14] B. Li, A. Pandolfi, and M. Ortiz. Material-point erosion simulation of dynamic fragmentation of metals. *Mechanics of Materials*, 80, Part B:288 – 297, 2015.

[15] T. LI, J.-J. Marigo, D. Guilbaud, and S. Potapov. Gradient damage modeling of brittle fracture in an explicit dynamics context. Submitted. hal-01248263, 2015.

[16] C. Linder and F. Armero. Finite elements with embedded branching. *Finite Elements in Analysis and Design*, 45(4):280 – 293, 2009.

[17] D. L. Linero. *A model of material failure for reinforced concrete via Continuum Strong Discontinuity Approach and mixing theory*. PhD thesis, E.T.S. Enginyers de Camins, Canals i Ports, Technical University of Catalonia (UPC), Barcelona, 2006. Cimne Monograph Nbr.M106.

[18] O. Lloberas-Valls, A. E. Huespe, J. Oliver, and I. F. Dias. Strain injection techniques in dynamic fracture modeling. *Computer Methods in Applied Mechanics and Engineering*, 2016. Submitted.

[19] C. Miehe, M. Hofacker, and F. Welschinger. A phase field model for rate-independent crack propagation: Robust algorithmic implementation based on operator splits. *Computer Methods in Applied Mechanics and Engineering*, 199(4548):2765–2778, 2010.

[20] J. Oliver. Continuum modelling of strong discontinuities in solid mechanics using damage models. *Computational Mechanics*, 17(1-2):49–61, 1995.

[21] J. Oliver. Modelling strong discontinuities in solids mechanics via strain softening constitutive equations. part 1: Fundamentals. *International Journal for Numerical Methods in Engineering*, 39(21):3575–3600, 1996.

[22] J. Oliver, A. E. Huespe, M. D. G. Pulido, and E. Chaves. From continuum mechanics to fracture mechanics: the strong discontinuity approach. *Engineering Fracture Mechanics*, 69:113–136, 2002.

[23] J. Oliver, I. F. Dias, and A. E. Huespe. Crack-path field and strain-injection techniques in computational modeling of propagating material failure. *Computer Methods in Applied Mechanics and Engineering*, 274:289–348, 2014.

[24] J. Oliver, M. Caicedo, E. Roubin, A. E. Huespe, and J. A. Hernández. Continuum approach to computational multiscale modeling of propagating fracture. *Computer Methods in Applied Mechanics and Engineering*, 294:384 – 427, 2015.

[25] J. Ožbolt, A. Sharma, and H.-W. Reinhardt. Dynamic fracture of concrete – compact tension specimen. *International Journal of Solids and Structures*, 48(10):1534 – 1543, 2011.

[26] A. Pandolfi, P. Krysl, and M. Ortiz. Finite element simulation of ring expansion and fragmentation: the capturing of length and time scales through cohesive models of fracture. *International Journal of Fracture*, 95(1–4):279–297, 1999.

[27] R. R. Pedersen, A. Simone, and L. J. Sluys. An analysis of dynamic fracture in concrete with a continuum visco-elastic visco-plastic damage model. *Engineering Fracture Mechanics*, 75(13):3782–3805, 2008.

[28] R. R. Pedersen, A. Simone, and L. J. Sluys. Mesoscopic modeling and simulation of the dynamic tensile behavior of concrete. *Cement and Concrete Research*, 50:74–87, 2013.

[29] M. Ramulu and A. S. Kobayashi. Mechanics of crack curving and branching a dynamic fracture analysis. *International Journal of Fracture*, 27(3-4):187–201, 1985.

[30] E. Sharon and J. Fineberg. Confirming the continuum theory of dynamic brittle fracture for fast cracks. *Nature*, 397(6717):333–335, 1999.

[31] E. Sharon, S. P. Gross, and J. Fineberg. Local crack branching as a mechanism for instability in dynamic fracture. *Physical Review Letters*, 74(25):5096–5099, 1995.

[32] S.A. Silling. Dynamic fracture modeling with a meshfree peridynamic code. In K. J. Bathe, editor, *Computational Fluid and Solid Mechanics 2003*, pages 641–644. Elsevier Science Ltd, Oxford, 2003.

[33] J. C. Simo and J. Oliver. A new approach to the analysis and simulation of strain softening in solids. *Fracture and damage in quasibrittle structures*, pages 25–39, 1994.

[34] J. C. Simo and M. S. Rifai. A class of mixed assumed strain methods and the method of incompatible modes. *International Journal for Numerical Methods in Engineering*, 29(8): 1595–1638, 1990.

[35] J.-H. Song and T. Belytschko. Cracking node method for dynamic fracture with finite elements. *International Journal for Numerical Methods in Engineering*, 77(3):360–385, 2009.

[36] J.-H. Song, H. Wang, and T. Belytschko. A comparative study on finite element methods for dynamic fracture. *Computational Mechanics*, 42(2):239–250, 2008.